Cauchy-characteristic evolution of Einstein-Klein-Gordon systems

Roberto Gómez,[1] Pablo Laguna,[2] Philippos Papadopoulos,[2] and Jeff Winicour[1]
[1]*Department of Physics and Astronomy, University of Pittsburgh, Pittsburgh, Pennsylvania 15260*
[2]*Department of Astronomy and Astrophysics and Center for Gravitational Physics and Geometry, Penn State University, University Park, Pennsylvania 16802*
(Received 4 April 1996)

A Cauchy-characteristic initial value problem for the Einstein-Klein-Gordon system with spherical symmetry is presented. Initial data are specified on the union of a spacelike and null hypersurface. The development of the data is obtained with the combination of a constrained Cauchy evolution in the interior domain and a characteristic evolution in the exterior, asymptotically flat region. The matching interface between the spacelike and characteristic foliations is constructed by imposing continuity conditions on metric, extrinsic curvature, and scalar field variables, ensuring smoothness across the matching surface. The accuracy of the method is established for all ranges of M/R, most notably, with a detailed comparison of invariant observables against reference solutions obtained with a calibrated, global, null algorithm. [S0556-2821(96)01120-4]

PACS number(s): 04.30.Nk, 04.25.Dm, 04.40.Nr

I. INTRODUCTION

The correct physical formulation of any asymptotically flat, radiative Cauchy problem requires boundary conditions at spatial infinity. These conditions ensure not only that total energy and the energy loss by radiation are both finite, but they are also responsible for the proper $1/r$ asymptotic falloff of the radiation fields. However, when treating radiative systems computationally, an outer boundary must be established artificially at some large but finite distance in the wave zone, i.e., many wavelengths from the source. Imposing an accurate radiation boundary condition at a finite distance is a difficult task even in the case of simple radiative systems evolving on a fixed geometric background. The problem is exacerbated when dealing with the Einstein equations.

In recent years, the characteristic initial value problem (cIVP) formulation of the Einstein equations in nonspherically symmetric configurations [1,2] has been explored, providing possible alternatives to the practical and theoretical problems introduced by the outer boundary conditions of the Cauchy initial value problem (CIVP). Based on the concept of combined Cauchy-characteristic evolution, a number of systems are currently under investigation. The motivation behind these new formulations of the initial value problem is to capture the advantages that each approach exhibits and at the same time avoid some of the corresponding drawbacks. The CIVP permits the construction of integration algorithms that allow null infinity to be included in a compactified grid, hence facilitating and clarifying the extraction of radiation. However, characteristic formulations generally break down in regions of complicated caustic structure, which are unavoidable in strongly asymmetric geometries such as those describing the merger of two black holes. Cauchy evolutions avoid this problem, yet they provide no natural way to impose conditions at the outer boundary. Since each method operates successfully precisely in the region where the other has its shortcomings, an appropriate matching of the two initial value formulations promises an effective approach to the outer boundary condition and the caustic problem.

The general idea behind the Cauchy-characteristic matching (CCM) is not entirely new. An early mathematical investigation exhibiting unions of spacelike and characteristic surfaces was given in [3]. Regarding general relativistic systems, a discussion of the potential of the method appears in [4]. The concept of a null exterior attached to a Cauchy evolution appears also in connection with perturbative approaches to the outer boundary problem, e.g., in [5] as well as in [6]. Yet, only recently [7–10], has the concept been carefully explored with respect to its practicability. A detailed study of the stability and accuracy of CCM for linear and nonlinear wave equations has been presented in [10,11], illustrating its potential for a wide range of wave systems. The numerical investigation of cylindrically symmetric solutions of the Einstein equations has also been carried out [4,9].

The objective of this paper is to develop and carefully calibrate the CCM method for asymptotically flat, spherically symmetric space-times, which are evolving in the presence of a minimally coupled, self-gravitating, massless scalar field. This is an initial step towards developing a general method applicable to the full Einstein equations. Research on this topic is stimulated and guided by the requirements of the Binary Black Hole Grand Challenge Alliance, a major collaboration aimed at the investigation of the merger of two in-spiraling black holes. The CCM approach will provide, in this context, both boundary conditions and radiation wave form extraction. The model problem investigated herein captures some essential aspects of the general system, including wave propagation on dynamical backgrounds and black-hole formation. The dynamics of the model is governed by the coupled Einstein-Klein-Gordon equations in spherical symmetry,

$$G_{ab}=\kappa(\nabla_a\Phi\nabla_b\Phi+Lg_{ab}), \tag{1}$$

and

$$\nabla_a\nabla^a\Phi=0, \tag{2}$$

where Φ is a scalar field whose Lagrangian is

$$L=-\frac{1}{2}\nabla_a\Phi\nabla^a\Phi \tag{3}$$

and $\kappa=8\pi$. (Units are chosen so that $G=c=1$.) Space-time indices are denoted with Latin letters $(a,b,c,\dots)$ and space indices with $(i,j,k,\dots)$.

This system has been studied intensively in the last five years both analytically [12] and numerically [13–17]. The existent understanding of the system is quite appropriate, as the exploration and calibration of the combined evolution is done in a nontrivial geometric setting, yet with good basic knowledge of the expected physical behavior.

The interior foliation and the associated integration algorithm are presented in Sec. II. The time integration is analogous to that used by Choptuik [18], the main difference being a different choice of boundary conditions. Section III describes the characteristic evolution algorithm. The method closely follows [13], with minor changes to accommodate the matching interface. In Sec. IV the geometric concepts underlying the matching theory are discussed, and a number of simplifying assumptions are put forward, which lead to a simple set of matching conditions for the problem at hand. The implementation of the combined evolution, along with validation tests, and numerical experiments covering a wide range of methodologies and physical parameters are given in Sec. V.

II. INTERIOR DOMAIN: CAUCHY EVOLUTION

For the interior (Cauchy) domain M^- of the four-dimensional space-time, Einstein's equations will be written using a standard $3+1$ Arnowitt-Deser-Misner (ADM) decomposition. Generally, a foliation of spacelike slices (hypersurfaces) is constructed and labeled by a scalar function τ. The unit normal to these slices is n^a. By construction, $n_a=-\alpha\nabla_a\tau$, where α is the lapse function. The intrinsic metric on each slice is then given by $\gamma_{ab}=g_{ab}+n_an_b$. The vector αn^a connects the slices of the foliation; however, this time vector is not unique. In general, the vector t^a can be chosen as $t^a=\alpha n^a+\beta^a$ where β^a is the shift vector and $\beta^a n_a=0$. Adopting this decomposition, the four-dimensional metric element in the case of spherically symmetric space-times reduces to the $3+1$ form

$$ds^2=(-\alpha^2+\beta^2e^{-2A})dt^2+2\beta dtd\rho+e^{2A}d\rho^2+\rho^2e^{2B}(d\theta^2+\sin^2\theta d\phi^2), \tag{4}$$

where $\beta\equiv\beta_\rho$ is the only nonzero component of the shift vector, and the metric on the spacelike hypersurfaces takes the form $\gamma_{ij}=\mathrm{diag}(e^{2A},\rho^2e^{2B},\rho^2e^{2B}\sin^2\theta)$. All the metric coefficients are functions only of ρ and t. The dynamical quantities in the $3+1$ initial value formulation are the intrinsic metric γ_{ab}, and the extrinsic curvature K_{ab}, of the slices. In spherical symmetry, the extrinsic curvature has only two independent components: $K^i_j=\mathrm{diag}(H_A,H_B,H_B)$.

The spatial projections of Einstein's equations lead to the evolution equations for the spatial tensors γ_{ij} and $K^i_j=\gamma^{ik}K_{kj}$:

$$A_{,t}=-\alpha H_A+e^{-2A}(\beta_{,\rho}-\beta A_{,\rho}), \tag{5}$$

$$B_{,t}=-\alpha H_B+e^{-2A}\beta\left(\frac{1}{\rho}+B_{,\rho}\right), \tag{6}$$

$$H_{A,t}=e^{-2A}[\alpha R_{\rho\rho}+\beta H_{A,\rho}-\alpha_{,\rho\rho}+A_{,\rho}\alpha_{,\rho}]+\alpha H_AK-\kappa[e^{-2A}(\Phi_{,\rho})^2], \tag{7}$$

$$H_{B,t}=e^{-2A}\left[\alpha\left(\frac{e^{2A-2B}}{\rho^2}\right)R_{\theta\theta}+\beta H_{B,\rho}-\alpha_{,\rho}\left(\frac{1}{\rho}+B_{,\rho}\right)\right]+\alpha H_BK, \tag{8}$$

where K denotes the trace K^i_i of the extrinsic curvature.

The time-time and time-space projections of the Einstein's equations yield, respectively, the Hamiltonian and momentum constraints

$$\frac{1}{2}R_{\rho\rho}+\frac{e^{2A-2B}}{\rho^2}R_{\theta\theta}+e^{2A}H_B(H_B+2H_A)=\frac{1}{2}\kappa[(\Phi_{,\rho})^2+e^{2A}\Pi^2] \tag{9}$$

and

$$H_{B,\rho}+\left(\frac{1}{\rho}+B_{,\rho}\right)(H_B-H_A)=\frac{1}{2}\kappa\Pi\Phi_{,\rho}, \tag{10}$$

where $R_{\rho\rho}$ and $R_{\theta\theta}$ are the three-Ricci components given by

$$\frac{1}{2}R_{\rho\rho}=-B_{,\rho\rho}+\frac{1}{\rho}(A_{,\rho}-2B_{,\rho})+B_{,\rho}(A_{,\rho}-B_{,\rho}), \tag{11}$$

$$\frac{e^{2A-2B}}{\rho^2}R_{\theta\theta}=-B_{,\rho\rho}+\frac{1}{\rho}(A_{,\rho}-4B_{,\rho})+B_{,\rho}(A_{,\rho}-2B_{,\rho})+\frac{1}{\rho^2}(e^{2A-2B}-1). \tag{12}$$

Finally, the $3+1$, first order in time, form of the Klein-Gordon equation (2) is

$$\Phi_{,t}=\alpha\Pi+e^{-2A}\beta\Phi_{,\rho}, \tag{13}$$

$$\Pi_{,t}=e^{-2A}\left\{\alpha\left[\frac{1}{\rho^2}(\rho^2\Phi_{,\rho})_{,\rho}+(2B_{,\rho}-A_{,\rho})\Phi_{,\rho}+e^{2A}K\Pi\right]+\alpha_{,\rho}\Phi_{,\rho}+\beta\Pi_{,\rho}\right\}. \tag{14}$$

The geometry evolution equations (5)–(8) together with the matter evolution equations (13) and (14) constitute an initial value problem for the quantities A,B,H_A,H_B,Φ,Π. The initial data for the IVP must satisfy the constraints (9) and (10). Obtaining the development of the initial data requires, furthermore, the specification of the gauge functions α and β. Ideally, the time integration of the IVP defined above should put no restrictions on either the form of the metric or the gauge functions. Yet the use of spherical coordinates, mandated by the Killing symmetries (and also computationally efficient), significantly limits the freedom to choose the space-time slicing. For example, the simplest pos-

sible gauge, the geodesic or synchronous gauge ($\alpha=1,\beta=0$), leads to a coupled system of equations for the geometric variables A,B,H_A,H_B. Formulating this problem as a set of second order equations for A,B reveals a dynamical structure that is not that of a wave system. In practice, this leads to considerable difficulties in preserving the appropriate regularity of the geometry near the origin. Such regularity is analytically ensured by cancellations of $1/r$ terms both explicitly in the right-hand side of the evolution equations and implicitly by the enforcement of the constraints.

A gauge choice that overcomes the regularity problems at the origin is the radial gauge, in which ρ is chosen such that the area of each $dt=d\rho=0$ sphere is equal to $4\pi\rho^2$, which leads to the condition $B=0$. The integration procedure outlined below also assumes a vanishing shift condition, but can be generalized for arbitrary shift.

The line element (4) with $B=\beta=0$ becomes

$$ds^2=-\alpha^2dt^2+e^{2A}d\rho^2+\rho^2(d\theta^2+\sin^2\theta d\phi^2). \quad (15)$$

As an immediate consequence of $B=\beta=0$, Eq. (6) implies that H_B also vanishes, and Eq. (8) for $H_{B,t}$ gives a condition on the lapse function:

$$\alpha_{,\rho}-\left[A_{,\rho}+\frac{1}{\rho}(e^{2A}-1)\right]\alpha=0. \quad (16)$$

Furthermore, Eqs. (5) and (7) reduce to

$$A_{,t}=-\alpha H_A, \quad (17)$$

$$H_{A,t}=e^{-2A}\left[\frac{2}{\rho}\alpha A_{,\rho}-\alpha_{,\rho\rho}+A_{,\rho}\alpha_{,\rho}\right]+\alpha H_A^2-\kappa e^{-2A}(\Phi_{,\rho})^2. \quad (18)$$

With the conditions $B=H_B=0$, the Hamiltonian and momentum constraints are now decoupled equations relating the metric function A and its associated extrinsic curvature H_A to the scalar field energy density and current, respectively:

$$A_{,\rho}+\frac{1}{2\rho}(e^{2A}-1)=\frac{1}{2}\kappa\rho[(\Phi_{,\rho})^2+e^{2A}\Pi^2], \quad (19)$$

$$H_A=-\frac{1}{2}\kappa\rho\Pi\Phi_{,\rho}. \quad (20)$$

Finally, the scalar field equations, in this gauge, take the form

$$\Phi_{,t}=\alpha\Pi, \quad (21)$$

$$\Pi_{,t}=\alpha e^{-A}\left[\frac{1}{\rho^2}(\rho^2\Phi_{,\rho})_{,\rho}-\frac{A_{,\rho}}{2}\Phi_{,\rho}+e^AH_A\Pi\right]+e^{-A}\alpha_{,\rho}\Phi_{,\rho}. \quad (22)$$

In summary, the lapse function is determined by the condition (16). The remaining gravitational variables (A and H_A) can be constructed from a subset of the evolution equations (17) and (18) and constraint equations (19) and (20). Different integration schemes can be designed depending on which two equations are chosen from (17)–(20) to solve for A and H_A. For instance, a free, unconstrained evolution consists of using Eqs. (17) and (18). On the other hand, a fully constrained evolution would require solving the Hamiltonian constraint (19), with the extrinsic curvature H_A computed from the source terms using Eq. (20). Alternatively, a mixed scheme can be followed, with H_A again given by Eq. (20), while the metric variable is updated using Eq. (17), subject again to the lapse condition. Still other alternative schemes involving combinations of Eqs. (17)–(20) are possible. A fully constrained evolution is adopted here since it has been used in earlier accurate calculations of scalar wave collapse [16] and facilitates enforcing a regular metric boundary condition at the origin.

In order to complete the IVP, specific boundary conditions for the scalar field variables Φ,Π at both ends of the integration domain must be prescribed, along with integration constants for the hypersurface equations (19) and (16). The scalar field variables must be finite at $\rho=0$, and thus the appropriate boundary conditions at this point are $\rho\Phi=\rho\Pi=0$. The outer boundary conditions for these variables are well understood only in the limit $\rho\to\infty$, where rigorous outgoing wave conditions exist. Imposing a boundary condition at any finite ρ involves a certain *physical* approximation. Achieving a complete solution of the IVP without such additional assumptions is indeed the main focus of the CCM program, and the details are given in Sec. IV.

The prescription of the integration constants for the hypersurface equations at some point ρ_0 relates the labeling of the time and radial coordinates with the proper time and radial distance measurements of a privileged observer. Two obvious choices are geodesic observers, either at the center of symmetry, or at the outer boundary. While the choice does not have any consequences on physical observables, it is more natural for our integration procedure to assume a geodetic observer at the center of symmetry, and hence to require that $A=\alpha=0$ there. In fact, this choice is well suited for the study of critical collapse as well, where the self-similar critical solution [15] manifests itself in terms of the proper time of an observer at the origin.

III. EXTERIOR DOMAIN: CHARACTERISTIC EVOLUTION

For the exterior characteristic evolution, a family of null hypersurfaces $u=$const is introduced, emanating along the outward normals to the cross sections of the matching world tube and labeled by $u=t$. The outgoing null rays are parametrized by an area coordinate r, with $r=R$ at the matching world tube. The coordinate $x=r/(R+r)$ is introduced for purposes of compactification, so that null infinity is located at $x=1$. (In the numerical simulations to be presented later, we set the scale so that $R=1$ and consequently $x=1/2$ at the matching world tube.) In the null coordinate system, the line element in the exterior region has the form [13]

$$ds^2=-e^{2\lambda}du\left(\frac{V}{r}du+2dr\right)+r^2(d\theta^2+\sin^2\theta d\phi^2), \quad (23)$$

where the metric functions λ and V depend only on u and r.

The hypersurface equations for λ and V are

$$\lambda_{,r}=2\pi r(\Phi_{,r})^2 \tag{24}$$

and

$$V_{,r}=e^{2\lambda}. \tag{25}$$

The scalar wave equation in the characteristic region takes the form

$$2(r\Phi_{,u})_{,r}=1r(rV\Phi_{,r})_{,r}. \tag{26}$$

In terms of the intrinsic metric of the (u,r) submanifold,

$$\eta_{\alpha\beta}dx^{\alpha}dx^{\beta}=-e^{2\lambda}du\left(\frac{V}{r}du+2dr\right), \tag{27}$$

where the greek indices take the values $(0,1)$, this reduces to

$$\Box^{(2)}g=\frac{e^{-2\lambda}g}{r}\left(\frac{V}{r}\right)_{,r}, \tag{28}$$

where $g=r\Phi$ and $\Box^{(2)}$ is the D'Alembertian associated with $\eta_{\alpha\beta}$.

The integration of the system (24)–(26) proceeds with the specification of initial data $\Phi(u_0,r)$ for $r>R$ on the initial null cone u_0. The hypersurface equations are integrated radially and furnish compatible geometric functions λ and V. This, in turn, allows the time integration of the scalar field equation, which provides new data in the neighborhood u_0+du and completes the integration cycle. The extra information needed to evolve the space-time is the characteristic initial data $\Phi(u,R)$ at the inner boundary, as well as the boundary values $\lambda(u,R)$ and $V(u,R)$. A characteristic integration algorithm for Eq. (28) may be based upon the null parallelogram made up of incoming and outgoing radial characteristics [19,2].

IV. CAUCHY-CHARACTERISTIC MATCHING

The match is performed across a three-dimensional, time-like hypersurface Σ (world tube), which divides the four-dimensional space-time into two disjoint sub-manifolds M^+ (characteristic exterior) and M^- (Cauchy interior). Each sub-manifold $M^{\pm}$ is endowed with a metric $g^{\pm}_{ab}$ that induces a unique intrinsic geometry at Σ. Independent coordinate charts $\{x^a\}^{\pm}$ are introduced in $M^{\pm}$. Let s^a be the space-like, unit normal to Σ directed from M^- to M^+. The metric intrinsic to Σ, is then given by

$$h_{ab}=g_{ab}-s_a s_b, \tag{29}$$

where h^a_b is the projection operator into the subspace Σ. The second fundamental form, or extrinsic curvature of Σ, is defined by

$$\Theta_{ab}=h^c_a h^d_b\nabla_{(c}s_{d)}. \tag{30}$$

If v^a is the time-like, unit tangent to Σ, the metric h_{ab} has the further decomposition

$$h_{ab}=-v_a v_b+R^2 q_{ab}, \tag{31}$$

where q_{ab} is the unit sphere metric. The metric tensors h_{ab},q_{ab} and the vectors s^a,v^a satisfy the following orthogonality conditions: $s^a h_{ab}=s^a q_{ab}=v^a q_{ab}=s^a v_a=0$.

The metric continuity requirement can be recast as conditions on the induced norm of the tangent vector v^a on Σ,

$$[v^a v^b g_{ab}]^-=[v^a v^b g_{ab}]^+ \tag{32}$$

and the surface-area radius,

$$[q^{ab}g_{ab}]^-=[q^{ab}g_{ab}]^+. \tag{33}$$

In addition to the continuity of the metric across Σ, in order to prevent sheet discontinuities (singular hypersurfaces), the following conditions on the extrinsic curvature must be imposed [20]:

$$[v^a v^b\Theta_{ab}]^-=[v^a v^b\Theta_{ab}]^+ \tag{34}$$

and

$$[q^{ab}\Theta_{ab}]^-=[q^{ab}\Theta_{ab}]^+. \tag{35}$$

Equations (32)–(35) should be understood as a limit process. Namely, for any tensor A_{ab}, the continuity condition $[A_{ab}]^-=[A_{ab}]^+$ implies

$$\lim_{Q\to P^-}A^-_{ab}(Q)=\lim_{O\to P^+}A^+_{ab}(O), \tag{36}$$

where $P^{\pm}\in\Sigma^{\pm}$ and $Q\to P^-$, $O\to P^+$, through M^-,M^+, respectively. The continuity condition (36) has meaning only if there exists a mapping $\mathcal{M}:\Sigma^-\to\Sigma^+$ which transforms tensor components between the two coordinate systems.

In the spherically symmetric case under consideration, the coordinate systems $\{t,\rho,\theta,\phi\}$ in M^- and $\{u,r,\theta,\phi\}$ in M^+ are introduced. Because of the symmetry, the same coordinates θ and ϕ are used everywhere throughout $M^{\pm}$. This is not the case with the radial coordinate. In general, ρ and r are not the same. The line elements in $M^{\pm}$ are given by Eqs. (15) and (23), respectively. The tangent vector to Σ in these coordinates is

$$v^a=\frac{dx^a}{d\tau}\equiv\dot{x}^a=\begin{cases}(\dot{t},\dot{\rho},0,0) & \text{in } M^-,\\ (\dot{u},\dot{r},0,0) & \text{in } M^+.\end{cases} \tag{37}$$

In this section, an overdot denotes derivative with respect to the proper time τ along the world tube Σ. That is $\dot{f}\equiv df/d\tau=v^a\partial_a f$. From $u^a s_a=0$ and $s^a s_a=1$, it follows that

$$s_a=\begin{cases}\alpha e^A(-\dot{\rho},\dot{t},0,0) & \text{in } M^-,\\ e^{2\lambda}(-\dot{r},\dot{u},0,0) & \text{in } M^+,\end{cases} \tag{38}$$

and

$$s^a=\begin{cases}\alpha^{-1}e^A(\dot{\rho},\alpha^2e^{-A}\dot{t},0,0) & \text{in } M^-,\\ (-\dot{u},\dot{r}+\dot{u}V/r,0,0) & \text{in } M^+.\end{cases} \tag{39}$$

The continuity conditions on the metric, Eqs. (32) and (33), can now be rewritten as

$$-\alpha^2\dot{t}^2+e^{2A}\dot{\rho}^2=-e^{2\lambda}(\dot{u}^2V/r+2\dot{u}\dot{r}) \tag{40}$$

and

$$\rho=r\equiv R, \tag{41}$$

respectively. Note that condition (32) applies only at $r=R$, where R is the surface-area radius of the matching surface. R is taken to be constant on Σ, hence the matching surface is invariant under the orbits of the spherical symmetry.

An additional assumption adopted here is that the matching surface does not move in coordinate space ($\dot{r}=\dot{\rho}=0$) and that the coordinate time in M^+ and M^- agree in Σ ($u=t$). The metric continuity condition (40) then reduces to

$$\alpha^2=e^{2\lambda}\frac{V}{R}, \tag{42}$$

with all functions evaluated at the matching surface.

Similarly, the continuity conditions on the extrinsic curvature, Eqs. (34) and (35), yield, respectively,

$$[q^{ab}\nabla_a s_b]^-=[q^{ab}\nabla_a s_b]^+ \tag{43}$$

and

$$[s^a a_a]^-=[s^a a_a]^+, \tag{44}$$

where $a^a=u^b\nabla_b u^a$ is the world tube ''acceleration.'' In spherical symmetry, condition (43) reduces to

$$[s^a\nabla_a R]^+=[s^a\nabla_a R]^-, \tag{45}$$

which can be rewritten using Eq. (39) explicitly in terms of the metric functions as

$$\frac{\alpha}{e^A}=\frac{V}{R}, \tag{46}$$

at the matching surface Σ.

The condition (44) yields an equation for $\ddot{t}$ from which the coordinate times, t or u, at Σ can be solved in terms of the proper time τ. Alternatively, $t(\tau)$ and $u(\tau)$ can be obtained from the normalization condition of v^a of s^a.

The matching of the scalar field variables across the two coordinate domains must ensure that neither the field values nor the field derivatives exhibit jump discontinuities on the interface. That is,

$$[\Phi]^-=[\Phi]^+ \tag{47}$$

and

$$[l^a\nabla_a\Phi]^-=[l^a\nabla_a\Phi]^+ \tag{48}$$

for any vector l^a. It is convenient to choose $l^a=s^a+v^a$, which is an outgoing null vector at Σ. In this case, the continuity equation at the matching surface becomes

$$\frac{\partial\Phi}{\partial t}+\alpha e^{-A}\frac{\partial\Phi}{\partial\rho}=\frac{V}{R}\frac{\partial\Phi}{\partial r}. \tag{49}$$

In the limit $R\to\infty$, for an asymptotically flat space-time with no incoming radiation, Eq. (49) reduces to the familiar Sommerfeld condition if the right-hand side of Eq. (49) is set to zero. However, unlike the Sommerfeld condition which is only valid asymptotically, Eq. (49) is an *exact* relation, valid at any distance.

For the momentum variable Π, the procedure is different, to avoid imposing continuity on higher derivatives at Σ. Starting from the definition $\Pi=v^a\nabla_a\Phi$, it is rewritten as

$$\Pi+s^a\nabla_a\Phi=l^a\nabla_a\Phi \tag{50}$$

which leads to the condition

$$e^A\Pi+\frac{\partial\Phi}{\partial\rho}=\frac{\partial\Phi}{\partial r}. \tag{51}$$

The system of Eqs. (42), (46), (49), and (51) completes the specification of the matching interface.

V. TESTS AND RESULTS

A. Stability and accuracy tests

The discretization algorithms in both domains, as well as the implementation of the continuity conditions are all constructed by replacing derivatives by second order accurate, centered finite differences. The matching surface lies at a fixed coordinate location, which is a grid point of both the ρ and r coordinate grids. This simple scheme leads to long term numerical stability, which is not an automatic feature of a matching algorithm [10]. Here, long term stability is defined as the bound evolution of initial data over time periods large compared to the light crossing time of the inner computational domain. This stability requirement is stronger than classical Von-Neumann stability, which requires bound local propagation of linearized modes. Such stability is becoming more and more important in numerical relativity as the desired integration times become longer. The CCM code developed in this work exhibited stability for evolution times at least three orders of magnitude larger than the light crossing time.

In Fig. 1 a typical matched evolution is shown for initial data with a relatively small M/R ratio (0.08). The functional dependence of the initial data is given in this case by a Gaussian,

$$r\Phi=\lambda e^{-((r-r_c)/\sigma)^2} \tag{52}$$

with $\lambda=0.0225$, $r_c=2.0$, and $\sigma=0.1$. The left column shows snapshots of the evolution in the Cauchy domain, with the radial coordinate ρ running from the origin $\rho=0$ to the matching radius $\rho=1$. The right column shows the corresponding null evolution, with the compactified radial coordinate x running from the matching radius $x=0.5$ to null infinity at $x=1$. The field variables illustrated in all snapshots are $\rho\Phi$ and $r\Phi$, with the scale being constant for plots in the same row.

The first row includes a few snapshots that follow an imploding pulse as it crosses the matching surface and propagates into the Cauchy domain. Note that at this instance, an inaccurate matching scheme would create back reflection which would immediately register at null infinity. The appar-

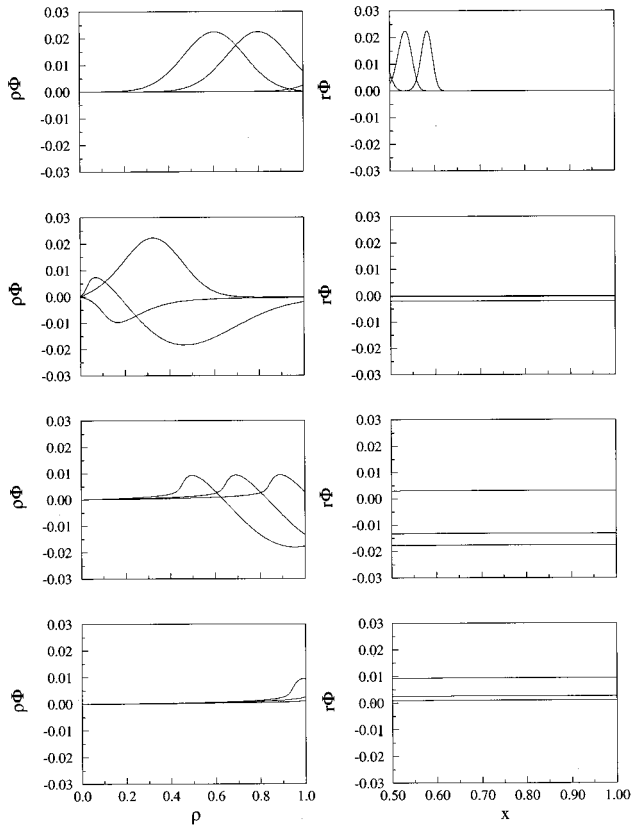

FIG. 1. CCM evolution. The left column depicts evolution in the Cauchy domain, the right column shows the corresponding null evolution. The field variables illustrated are $\rho\Phi$ and $r\Phi$, respectively. For each row, the left-hand scale gives the amplitude in the two domains.

ent widening of the pulse as it enters the Cauchy region is due to the different radial functions used in the two coordinate systems as well as the doubling of the local propagation speed in the Cauchy sector. The second row demonstrates the propagation and reflection of the (marginally subcritical) pulse off the origin. Strong nonlinear distortions occur there, while the leading part of the pulse is already crossing the matching surface and radiating to null infinity. In the third row, the peak of the pulse is propagating outward across the matching surface; and the solution finally decays in the fourth row, as the trailing parts of the pulse cross Σ. The very slight curvature of the pulse in the null region, as the peak amplitude crosses the matching surface, indicates a small amount of backscattering occurring at this time.

Second order convergence of all computed quantities to a limiting value is readily verified, e.g., by monitoring the final field configuration for a sequence of successively refined grids. A more physically intuitive test, the conservation of the total energy of the system, is a powerful probe into how well the discretization of the Einstein equations preserves the additional differential structure encoded in the Bianchi identities. A test of the absolute convergence of the energy residual ΔM is performed for that purpose. The energy residual between two time levels u_1, u_2 is defined as

$$\Delta M(u_1,u_2)=M(u_1)-M(u_2)+\int_{u_1}^{u_2}P(u)du, \qquad (53)$$

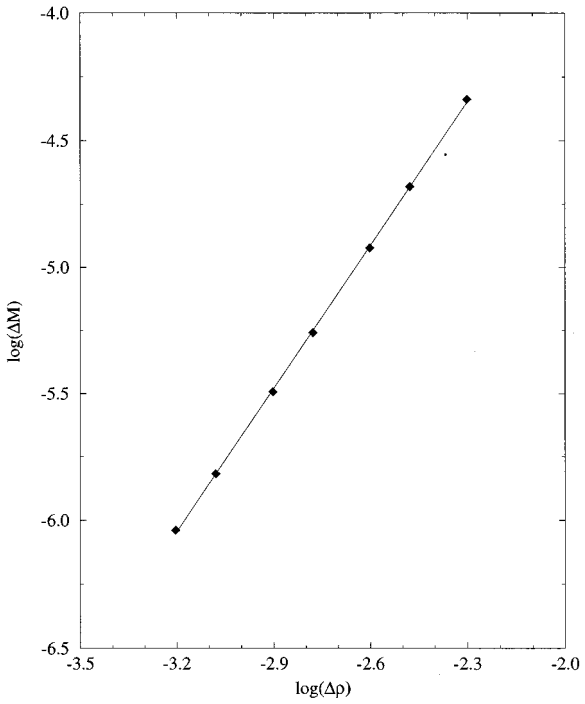

FIG. 2. Convergence test for the energy residual ΔM. The grid size $\Delta\rho$ refers to the Cauchy sector. The sequence of successive higher resolutions maintains a fixed ratio of the null sector grid size (Δr) to that of the Cauchy sector grid size $(\Delta\rho)$. The convergence rate for the demonstrated sequence of grid resolutions is 1.89. The logarithm is to base 10.

where $M(u)$ is the Bondi mass content of the space-time slice at time u while $P(u)$ is the power flow at infinity. ΔM is identically zero in the continuum limit and thus must converge to zero appropriately as a function of the discretization length-scale Δ.

The explicit forms of the Bondi mass M and the radiated power P in terms of metric quantities are given by

$$M(u)=\frac{1}{2}e^{-2H}r^2\left(\frac{V}{r}\right)_{,r}\Bigg|_{\infty}, \qquad (54)$$

$$P(u)=-4\pi e^{-2H}Q_{,u}^2, \qquad (55)$$

where $H(u)=\lim_{r\to\infty}\lambda(u,r)$ and $Q(u)=\lim_{r\to\infty}r\Phi(u,r)$.

In Fig. 2 the convergence of the energy residual is demonstrated. A sequence of approximate solutions with progressively finer resolution are obtained. The initial data (52) are prescribed in the null sector, while the Cauchy sector is taken to be flat initially. The Bondi mass is computed at the initial Bondi time $u_1=0$ and at a fixed final Bondi time $u_2=4.0$, while the power integral is accumulated (to second order accuracy) at each integration step. The second order convergence of the energy residual, consistent with the second order discretization of the component algorithms and the matching interface, is evidence of a successful matching of the two evolution schemes. The computational error in the mass and, most importantly, in the radiated power is directly controlled by the grid spacing Δ, and, in fact, diminishes as Δ^2.

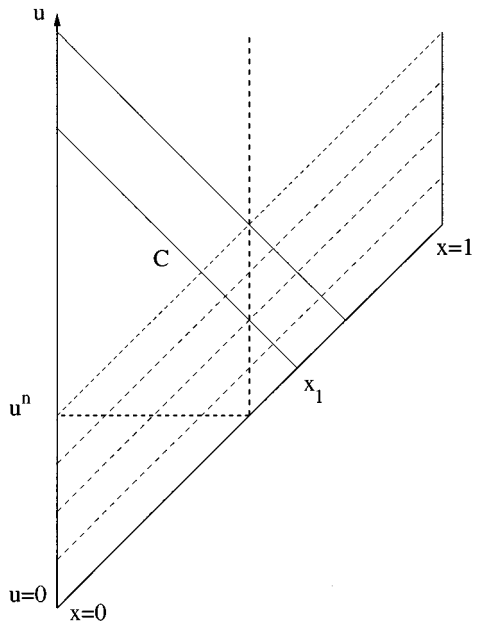

FIG. 3. The foliation of an asymptotically flat spherically symmetric space-time by outgoing null cones emanating from the origin. The initial data have compact support outside x_1 so that the inner region of the space-time (bounded above by C) is flat. The vertical and horizontal dotted lines give the location of the matching radius and the initial data surface of the comparison CCM run.

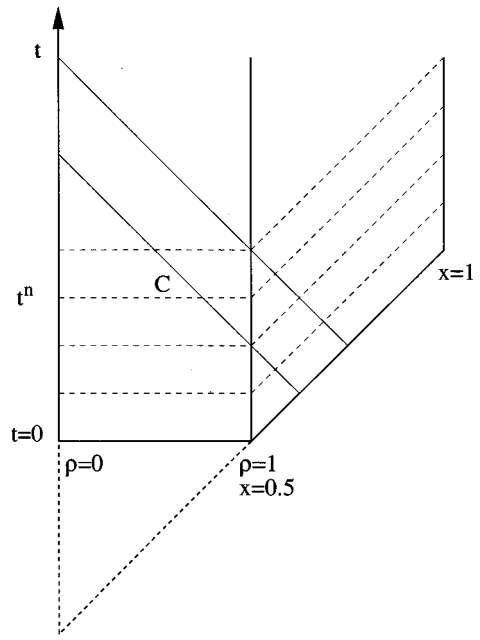

FIG. 4. The foliation of an asymptotically flat spherically symmetric space-time with a combination of spacelike and null hypersurfaces. Initial data for the comparison with the globally null code are given outside the matching surface. Flat Cauchy data in the interior complete the specification of a physical system.

B. Computing a space-time with two alternative foliations

A comparison of the numerical solution obtained by two, considerably different foliations of our model space-time is illustrated next. First, a calibrated characteristic code [16] is used to obtain a global evolution of initial data corresponding to an incoming wave with support outside a radius $x_1 = r_1/(1+r_1)$ (Fig. 3). This one-dimensional characteristic evolution will supply the wave form of the outgoing radiation coming back out to future null infinity. Since the initial data have compact support outside x_1, the space-time portion delimited by the initial time ($u=0$) surface, the origin world line $x=0$ and the incoming null cone C (beginning at x_1) will be flat.

Next, the CCM code, with a matching radius at $x=1/2<x_1$, is used to evolve the same characteristic data, along with flat-space Cauchy data on the initial time ($t=0$) surface (Fig. 4). The incoming pulse enters the Cauchy region across the matching surface in the inward direction, then gets Cauchy evolved until it leaves the matching surface in the outward direction and ends up at future null infinity. This test compares the wave forms at null infinity produced by a global null code and by a CCM code. Theoretically, the general covariance of the equations guarantees that the output should be identical. In practice, this test checks a combined algorithm (CCM) against a well-calibrated scheme, i.e., the one produced by the global null algorithm.

The wave forms are compared at null infinity, as would be measured by asymptotic (Bondi) observers. However, the time coordinates are considerably different for the two evolution schemes. In the CCM approach, the central time parametrizes the spacelike foliation with the proper time of an observer at the center of symmetry. This parametrization subsequently also labels the outgoing null cone foliation of the outer region of the space-time, with the synchronization performed at the matching radius. In contrast, the time parameter of the null foliation follows the proper time of the central observer, directly labeling the outgoing null cones emanating from the center of symmetry. Before comparing the two signals $(g_{\mathrm{CCM}}(t), g_N(u))$ they must be reparametrized according to the asymptotic Bondi time.

In a Bondi frame, geodesic observers would measure an asymptotically Lorentzian line element, which in the characteristic coordinate system is

$$ds^2 = -d\tilde{u}^2 - 2d\tilde{u}dr + r^2(d\theta^2 + \sin^2\theta d\phi^2). \quad (56)$$

The Bondi time $\tilde{u}$ is related to the coordinate time u of a general null cone foliation by the factor

$$\frac{d\tilde{u}}{du} = e^{2H(u)}, \quad (57)$$

defined following Eq. (55).

In Fig. 5 the signals at null infinity and their difference are shown as a function of Bondi time. The initial (characteristic) data are

$$\Phi = \Lambda r^2 e^{-(r-r_c)^2/\sigma^2} \sin kr \quad (58)$$

with the parameters for this plot being $\Lambda = 6\times10^{-4}$, $r_c = 3.0$, $\sigma = 0.6$, and $k = 10$. This value of Λ is just below the threshold of black-hole formation (which occurs at about $\Lambda = 6.125\times10^{-4}$) and leads to the strong distortion of the signal in the second half of the pulse. The signals obtained

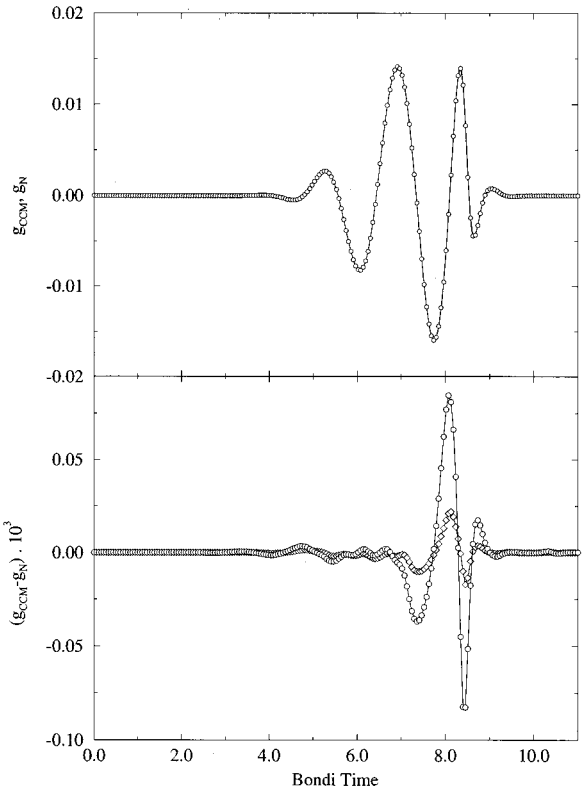

FIG. 5. Comparison of null and CCM evolutions in the case of subcritical initial data. The upper plot demonstrates the nearly identical signal at null infinity. The solid line shows the signal output of the CCM code, while the circles indicate the corresponding null code output at the same Bondi time. The lower plot highlights the difference in the signals. The signal difference for a CCM grid of 500+500 points and a null grid of 1000 points, is illustrated by the circle line. The diamond line shows the second order reduction of the difference when the resolution of all grids is doubled.

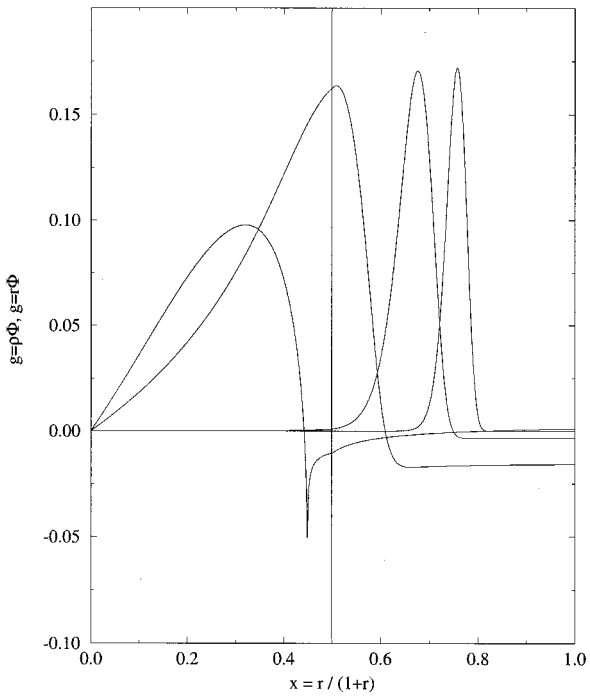

FIG. 6. CCM evolution and black-hole formation. The evolution of sufficiently strong Gaussian initial data leads to the formation of an apparent horizon, in this case at about $\rho=0.8$ ($x=0.45$). This is just marginally inside the matching radius at $\rho=1$ ($x=0.5$). The incoming Gaussian pulse (right side of the plot) propagates inwards (to the left), crosses the matching surface, and collapses, forming a cusplike profile.

with the two codes overlayed as functions of Bondi time show little difference to graphical accuracy, a manifestation of physical covariance and algorithmic compliance. The grid sizes used for this run were 500+500 points for the CCM code, and 1000 for the null code. The relative difference between the two signals for those resolutions is at the level of 0.1%. The maximum absolute value difference between the two signals over the total integration time provides a strong and physically interesting norm. This norm converges to zero with a measured rate of 1.99, consistent with the anticipated second order convergence.

The investigation is now extended to strong field phenomena, with the study of initial data that end up in the formation of a black hole. In the Cauchy region, black-hole formation is signaled when $e^{2A}\to\infty$ and the function $2m/r=1-e^{-2A}\to 1$ at some radius $R_{\rm BH}$. The mass of the black hole is then $M_{\rm BH}=2R_{\rm BH}$. Alternatively, the behavior of the lapse function, or the scalar field values themselves, can be used for similar estimates. In comparison, the formation of the black hole in the null region is signaled by the infinite redshift between Bondi time and coordinate time for all $r>R_{\rm BH}$, and the resulting decay of further radiative loss to infinity. The final value of the Bondi mass is then equal to $M_{\rm BH}$.

In practice, the evolution of the system cannot proceed accurately long after the black hole has formed. The use of a surface area coordinate r leads to a coordinate singularity inside the horizon [12] and the premise of the validity of the finite difference approximation breaks down. This is reflected, for example, in the breakdown of the convergence properties of the algorithm. Nevertheless, the matching procedure is sufficiently accurate to allow an investigation of black-hole formation quite close to the matching surface. (The mass of the black hole, and consequently the $M_{\rm BH}/R$ ratio, is controlled directly by the parametrization of the initial data.)

Figure 6 shows the evolution of a strong Gaussian pulse, leading to a black hole that has a mass only slightly smaller than the mass scale set by the matching radius ($R=1$). For demonstration purposes, the radial coordinate ρ is also compactified here, and the field functions are shown as if they were defined on a single grid. The highly nonlinear pulse creates strongly back-scattered radiation as it propagates inwards, but not enough to avoid a black-hole collapse. The discontinuity of the field derivatives at the location of the horizon is prominent in the late time snapshot.

Figure 7 displays the effects of black-hole formation on the time development of the wave form and of the Bondi mass. The initial data for those runs are given by Eq. (58) with the amplitude Λ increased progressively from 5.50×10^{-4} to 6.25×10^{-4} in three steps. Up until Bondi time of about 7.0, an increase in the amplitude of the initial data leads to a near linear increase of the initial mass (lower

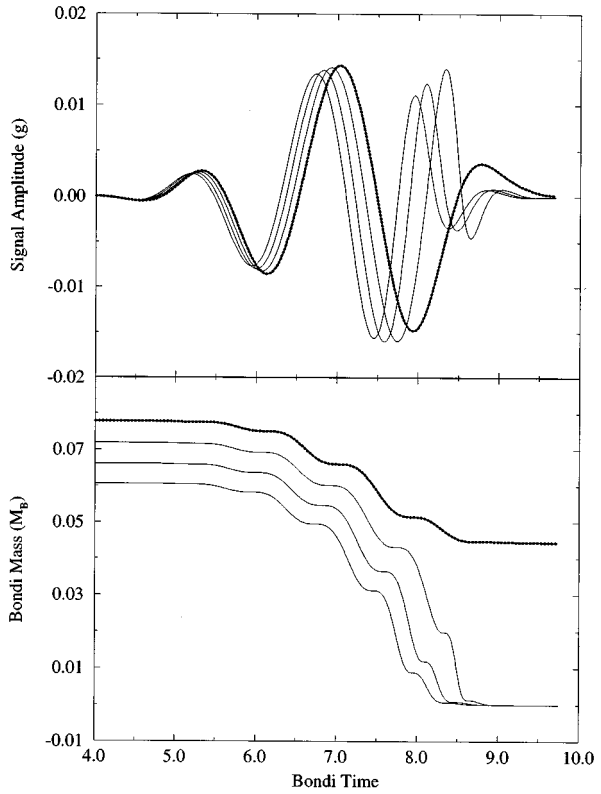

FIG. 7. The distortion of the signal at infinity for a space-time that develops a black-hole. The upper plot shows overlapping signals with a progression of initial amplitudes. The dotted signal corresponds to black-hole formation. The lower plot shows the evolution of the total Bondi mass.

plot) and to a corresponding redshifting of the wave form. Afterwards, there is a bifurcation point, at which data that lead to a black-hole space-time produce a signal severely distorted with respect to that of noncollapsing data. The Bondi mass either drops to zero for an asymptotically Minkowskian space-time, or coasts to a constant value that represents the mass of the newly formed black hole.

VI. CONCLUSION

The model problem of the self-gravitating scalar field provides a convenient framework for the study of the CCM research program in a controlled situation. It has been demonstrated here that the matched evolution is essentially transparent to the presence of the interface. The targets of (1) clearly identified radiative quantities and (2) physically accurate boundary conditions are achieved in this case with minimal computational and developmental effort. Direct application of the continuity conditions at the matching interface leads to a stable and accurate mixed evolution algorithm for all relevant M/R ratios. Although idealized, this model problem captures many essential physical aspects of more generic asymptotically flat space-times. It is expected that the geometrical approach and the algorithmic methodology initiated here are applicable and useful in more realistic problems, and work is currently under way exploring this possibility.

ACKNOWLEDGMENTS

We thank M. Choptuik and E. Seidel for helpful discussions of origin singularities in spherically symmetric systems. This work was supported by the Binary Black Hole Grand Challenge Alliance, NSF PHY/ASC 9318152 (ARPA supplemented) and NSF PHY 9510895 to the University of Pittsburgh. P.L. was supported in part by NSF Young Investigator Grant No. PHY 93-57219 and NSF Grant No. PHY 93-09834. Computer time for this project was provided by the Pittsburgh Supercomputing Center under PHY860023P to J.W.

[1] R. Isaacson, J. Welling, and J. Winicour, J. Math. Phys. (N.Y.) **24**, 7 (1983).
[2] R. Gómez, P. Papadopoulos, and J. Winicour, J. Math. Phys. (N.Y.) **35**, 8 (1994).
[3] G. Duff, Can. J. Math. **10**, 127 (1958).
[4] N. Bishop, *Approaches to Numerical Relativity*, edited by R. d'Inverno (Cambridge University Press, Cambridge, England, 1992).
[5] E. Seidel, Phys. Rev. D **42**, 6 (1990).
[6] J. Anderson and D. Hobill, in *Dynamical Space-times and Numerical Relativity*, Proceedings of the Workshop, Philadelphia, Pennsylvania, 1985, edited by J. M. Centrella (Cambridge University Press, Cambridge, England, 1986).
[7] C. Clarke and R. d'Inverno, Class. Quantum Grav. **11**, 1463 (1994).
[8] C. Clarke, R. d'Inverno, and J. Vickers, Phys. Rev. D **52**, 6863 (1995).
[9] M. Dubal, R. d'Inverno, and C. Clarke, Phys. Rev. D **52**, 6868 (1995).
[10] N. Bishop, R. Gómez, P. Holvorcem, R. Matzner, P. Papadopoulos, and J. Winicour, Phys. Rev. Lett. **76**, 4303 (1996).
[11] N. Bishop, R. Gómez, P. Holvorcem, R. Matzner, P. Papadopoulos, and J. Winicour (unpublished).
[12] D. Christodoulou, Commun. Math. Phys. **109**, 613 (1987).
[13] R. Gómez and J. Winicour, J. Math. Phys. (N.Y.) **33,** 4 (1992).
[14] C. Gundlach, R. Price, and J. Pullin, Phys. Rev. D **49**, 890 (1994).
[15] M. Choptuik, Phys. Rev. Lett. **70**, 1 (1993).
[16] D. Goldwirth and T. Piran, Phys. Rev. D **40**, 3263 (1989).
[17] M. Choptuik, D. Goldwirth, and T. Piran, Class. Quantum Grav. **9**, 721 (1992).
[18] M. Choptuik, Technical report, University of Texas at Austin, 1994 (unpublished).
[19] R. Gómez, J. Winicour, and R. Isaacson, J. Comput. Phys. **98**, 11 (1992).
[20] W. Israel, Nuovo Cimento **44B**, 1 (1996); **49B**, 463(E) (1967).